PCCP

ROYAL SOCIETY OF CHEMISTRY

PAPER

View Article Online
View Journal | View Issue

Cite this: *Phys. Chem. Chem. Phys.*, 2020, **22**, 9815

What does carbon tolerant really mean? *Operando* vibrational studies of carbon accumulation on novel solid oxide fuel cell anodes prepared by infiltration†

Martha M. Welander,‡[a] Daniel B. Drasbæk,‡[b] Marie L. Traulsen,[b] Bhaskar R. Sudireddy,[b] Peter Holtappels*[b] and Robert A. Walker *[ac]

Received 13th January 2020,
Accepted 8th April 2020

DOI: 10.1039/d0cp00195c

rsc.li/pccp

Operando Raman spectroscopy and electrochemical techniques were used to examine carbon deposition on niobium doped $SrTiO_3$ (STN) based SOFC anodes infiltrated with Ni, Co, $Ce_{0.9}Gd_{0.1}O_2$ (CGO) and combinations of these materials. Cells were operated with CH_4/CO_2 mixtures at 750 °C. Raman data shows that carbon forms on all cells under operating conditions when Ni is present as an infiltrate. Additional experiments performed during cell cool down, and on separate material pellets (not subject to an applied potential), show that chemically labile oxygen available in the CGO infiltrate will preferentially oxidize all deposited surface carbon as temperatures drop below 700 °C. These observations highlight the benefit of CGO as a material in SOFC anodes but more importantly, the value of *operando* spectroscopic techniques as a tool when evaluating a material's susceptibility to carbon accumulation. Solely relying on *ex situ* measurements will potentially lead to false conclusions about the studied materials' ability to resist carbon and improperly inform efforts to develop mechanisms describing electrochemical oxidation and material degradation mechanisms in these high temperature energy conversion devices.

Introduction

High temperature energy conversion systems such as solid oxide cells (SOCs) are an attractive technology for efficient energy conversion as they can operate in both fuel cell and electrolysis modes creating a self-contained energy system with net zero emissions when coupled with renewable fuel sources. When operated as a solid oxide fuel cell (SOFC), these devices have a higher electrical efficiency relative to commercially available low temperature proton exchange membrane fuel cells (PEMFCs), and can approach efficiencies of 90% in combined heat and power applications.[1–5] Their real advantage, however, is their fuel flexibility. Because SOFCs typically operate at temperatures above 600 °C with non-precious metal catalysts, they can use a wide range of carbon-containing fuels including CH_4, syngas, biogas, and higher molecular weight hydrocarbons. In order to leverage this advantage, however, SOFC anodes must be resistant to carbon accumulation (also known as coking) during operation. The traditional SOFC anode uses Ni as its electrocatalyst, and in SOFCs anode coking can take the form of carbon filaments, highly ordered graphite or disordered graphite. While small amounts of carbon have proven to be beneficial in some circumstances,[6–9] more extensive carbon accumulation leads to electrode failure by both impeding gas transport and blocking catalytically active sites, thereby limit the cell performance.[6,10] Additionally, irreversible metal dusting caused by carbon reacting with the Ni itself can occur leading to complete anode disintegration.[11] As a result of Ni's susceptibility to carbon-induced degradation, development of carbon tolerant, conducting materials has become a priority for SOFC development and high temperature materials research.

Commercial SOFC anodes are typically composed of a nickel and yttria stabilized zirconia cermet (Ni–YSZ) in order to provide both electrical and ionic conductivity as well as a thermal expansion coefficient match to the electrolyte. As an electrocatalyst Ni is affordable, stable under typical operating conditions, and offers exceptional electrical conductivity and catalytic activity compared to other anode candidates.[3,12–14]

[a] *Department of Chemistry & Biochemistry, Montana State University, P. O. Box, 173400, Bozeman MT 59715, USA. E-mail: rawalker@montana.edu*
[b] *Department of Energy Conversion and Storage, Technical University of Denmark, Building 310, Fysikvej 1, 2800 Kgs, Lyngby, Denmark*
[c] *Montana Materials Science Program, Montana State University, P. O. Box, 173400, Bozeman MT 59715, USA*

† Electronic supplementary information (ESI) available. See DOI: 10.1039/d0cp00195c

‡ Both authors contributed equally to this study.

Despite these benefits, however, Ni's high efficiency for C–H bond activation leaves the anode susceptible to carbon accumulation. Adding steam to the fuel mitigates carbon formation[15,16] but at the risk of oxidizing the Ni and limiting overall performance by decreasing the device's operating voltage. Additionally, Ni has been shown to drive carbon accumulation even under conditions not predicted by thermodynamics including for steam to carbon ratios >1.[9] Another alternative for mitigating carbon formation is to reform the hydrocarbon fuel upstream of the fuel cell. This additional fuel processing, however, lowers overall cell efficiency.[17] Consequently, numerous efforts have been devoted to developing materials-based solutions that prevent – or at least limit – carbon accumulation on fuel cell anodes. These tactics have ranged from complete replacement of the original Ni–YSZ cermet to more subtle material modifications.[18–20]

Materials such as copper, ceria, and mixed ionic electronic conducting (MIEC) perovskites are unable to match Ni's catalytic activity, but these materials have shown promise in their ability to operate directly with hydrocarbons fuels.[21–24] While high anode catalytic activity is important, improved carbon tolerance could arguably compensate for performance losses. In this context, 'carbon tolerant' describes high temperature anodes that do not suffer from coke formation when operating with hydrocarbon fuels. Perovskite materials stand out as possible replacements for Ni–YSZ cermet anodes. One example is donor-doped, strontium titanate ($SrTiO_3$, STO). Doped-STO materials have relatively high electronic conductivity and stability under reducing atmospheres, as well as tolerance to both carbon and sulfur.[25–28] STO's main drawback is its low electrocatalytic activity, ionic conductivity and correspondingly poor performance as a fully functional anode. A number of studies have added electrocatalytically active infiltrates such as Pd or Ni, together with oxygen ion conducting $Ce_{0.9}Gd_{0.1}O_2$ (CGO) to STO electrodes and have reported reasonable performance compared to state of the art Ni–YSZ anodes.[28,29]

The studies described below investigate whether or not niobium doped-STO (STN) anode scaffolds infiltrated with mixtures of nano-sized catalysts are truly carbon-tolerant. The use of nano-sized catalysts has multiple benefits although their effects are limited by coarsening at SOFC-relevant operating temperatures. In principle, cermet anodes would be most efficient if they consisted of a percolated network of nano-scale catalyst particles.[30,31] Material combinations of Ni, Co and CGO were used as catalysts as these materials have demonstrated carbon tolerance under open circuit and single atmosphere conditions in previous work.[32] Additionally, CGO based catalysts have been one of the most extensively studied anode materials for SOFCs operating directly with hydrocarbon fuels.[8,21,33–35] Many studies have claimed good performance with Ce based systems with little to no reported carbon accumulation.[36–43] These same studies, however, base their claims largely on indirect or *post mortem* analyses of whether or not carbon is observed on the decommissioned anodes.

Findings presented in this work employ *operando* vibrational Raman spectroscopy to explore directly carbon formation on functioning STN electrodes infiltrated with CGO, Ni and Co and combinations of these materials at 750 °C under varying atmosphere and electrochemical conditions. Data show that in anodes containing infiltrated Ni, either by itself or in combination with other nanocatalysts, carbon accumulates when exposed to CH_4. Carbon persists on STN anodes infiltrated solely with Ni when the anode is cooled to room temperature. On STN anodes co-infiltrated with either Ni–CGO or Ni–Co–CGO, however, observed carbon that forms at operational temperatures disappears as the cell cools. Additional experiments using simple material pellets show that while carbon can be homogenously distributed across an anode at operating temperatures, oxygen available in CGO remains chemically labile during cool-down and oxidizes deposited carbon leading to the false impression that the anodes were resistant to coking during operation. These findings, therefore, highlight the importance of using *operando* optical techniques when drawing conclusions about a material's carbon tolerance.

Experimental

The SOFCs used in this work were electrolyte-supported cells. The Sc_2O_3, stabilized ZrO_2 electrolyte (Nippon Shokubai Co., Ltd, Japan) of *ca.* 150 μm thickness was laser cut to 26 mm diameter. Onto this electrolyte, a $Sr_{0.94}Ti_{0.9}Nb_{0.1}O_3$ (STN) porous backbone was deposited through spray deposition. The slurry for the deposition was prepared using STN powder (prepared in the lab through solid state mixed oxide method), $PVP_{10\,000}$ dispersant/binder and ethanol solvent. After deposition, the backbone was sintered in air at 1200 °C for 8 hours. Subsequently, a $La_{0.6}Sr_{0.4}CoO_3$ (LSC) (Kusaka, Japan) – $Ce_{0.9}Gd_{0.1}O_2$ (CGO) (Rhodia GmbH, Germany) composite cathode was screen-printed on the opposite side of the electrolyte and sintered in air at 930 °C for 24 hours. Anode electrocatalysts comprised of Ni or Co or Ni–Co and CGO were added to the STN backbone by infiltration. The infiltration solutions were prepared in the following way: first, a 3 M CGO aqueous solution was prepared using corresponding metal nitrates. To this solution, nitrate precursors of the Ni or Co or Ni–Co metals were added in the ration of 90 : 10 by mass (CGO : metal). The full procedure for infiltration is described elsewhere.[44] After infiltration, the cells were calcined at 350 °C for 2 hours to decompose the metal nitrates. Finally, a cathode current collection layer, LSC, was screen-printed on the LSC–CGO cathode. A schematic diagram of the completed cells can be seen in Fig. 1 together with an SEM

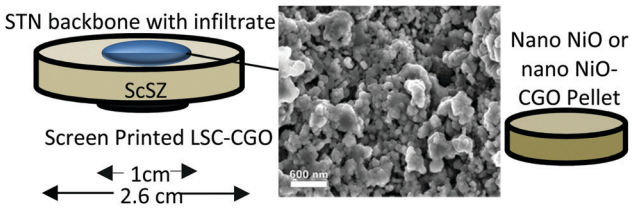

Fig. 1 Schematic representation of membrane electrode assemblies (with accompanying SEM image) and chip materials used for experiments.

Table 1 Summary of membrane electrode assemblies with catalyst loading percentages and the mass gained by infiltration

Sample name	Catalyst	Loading (wt%)	Mass gain (mg)
Ni	Ni	100	0.50 ± 0.2
Ni–CGO	Ni; CGO	10; 90	0.78 ± 0.08
Co–CGO	Co; CGO	10; 90	0.63 ± 0.24
Ni–Co–CGO	Ni; Co; CGO	5; 5; 90	0.58 ± 0.33
Ni–Co–CGO	Ni; Co; CGO	10; 10; 80	0.40 ± 0.12
Ni–YSZ	Ni; YSZ	40; 60	n/a

image of the infiltrated anode. A corresponding list of the complete fuel cell samples is shown in Table 1 below.

Current collectors consisting of gold wire (Alfa Aesar) attached to a gold mesh (Alfa Aesar) were attached to both electrodes with gold paste (Heraeus). The cells were then attached to a 2.6 mm diameter YSZ tube using ceramic paste (Aremco Products Inc.). The YSZ tube was enclosed in a quartz tube and sealed with a rubber stopper. Detailed descriptions of the experimental set up can be found in previous publications.[45,46] The assembly was then placed into a tube furnace for heating. Raman spectra were acquired using a Renishaw InVia spectrometer coupled to a 488 nm Ar-ion laser with 30–60 seconds exposures. Raman spectra were acquired using 100% of 30 mW laser power. The set laser power of was chosen to not risk photodegrading the studied materials and products. Backscattered light was directed through an edge filter with a 150 cm^{-1} low frequency cut off. Table 2 presents Raman modes and main peak assignments of the materials discussed in the Results section below. Electrochemical measurements were collected using a Princeton Applied Research VersaStat MC.

All cells were heated to 750 °C ± 5 °C at a ramp rate of 1 °C min^{-1} under 20 sccm Ar on the anode and 20 sccm air on the cathode. Once at temperature, gas flows were increased to 100 sccm Ar and 85 sccm air. Anodes were then reduced under 100 sccm humidified H_2 (3% H_2O) and anodes were considered fully reduced when the open circuit voltage stopped changing (−1.10 V). Once the anode was reduced, benchmark electrochemical measurements were performed including linear sweep voltammetry (LSV) and electrochemical impedance spectroscopy (EIS) (with humidified H_2). EIS measurements were collected with an AC voltage amplitude of 0.001 V over a frequency range of 1 MHz to 0.1 Hz. LSV measurements were carried out between 100% and 20% of the measured OCV in order to avoid cell damage and were collected using a sweep rate of 0.1 V s^{-1}.

Table 2 Raman modes and peak assignments, with literature references, of materials present in Results below. Frequencies are accurate to ±3 cm^{-1}

Phase/species	Raman modes	Main peak(s) room temperature (cm^{-1})
YSZ	F_{2g}	619[47]
CGO	F_{2g}	463[48]
NiO (nano)	LO	500[49]
NiO (micron)	2LO, (2M)	1090, (1490)[47]
STO	TO	415, 780[32]
C (graphite)	E_{2g}	1350, 1585, 2700[50]

Carbon exposure experiments were performed under 4 different anode atmospheres of varying CO_2 and CH_4 compositions totalling a flowrate of 100 sccm: 70% CO_2/30% CH_4, 50% CO_2/50% CH_4, 25% CO_2/75% CH_4, and 100% CH_4. Because polarization conditions can influence carbon deposition[51,52] in addition to CH_4–CO_2 ratios, EIS measurements were collected under each gas composition at 3 fixed current conditions including polarization of 85%, 40%, and 10% of the maximum current density obtained by the LSV. The effects of STN infiltration and carbon accumulation on cell electrochemical performance will be addressed in a future report. Raman kinetic measurements were collected for each set of conditions with 30 second exposure times. All Raman data were subject to instrument baseline and cosmic ray corrections. Carbon removal between sets was carried out using humidified Ar followed by reduction and benchmark measurements under humidified H_2. This procedure was performed between different gas compositions even when carbon was not observed. All cells were cooled under Ar in order to preserve the chemical composition of species across the anode for post-operation *ex situ* Raman spectroscopy.

Materials used for chip studies (Fig. 1) included commercially available nano-NiO and CGO powders (JT Baker). Pellets were pressed with a 1.27 cm diameter from either 100% NiO powder or mixture of 10 wt% CGO ($Gd_{0.2}Ce_{0.8}0_{1.95}$) and 90 wt% NiO. Pellets were sintered at 1400 °C with a ramp rate of 5 °C min^{-1} and a 1 hour dwell time. Chips from sintered pellets were attached to a closed YSZ disc using a small amount of ceramic paste (Aremco Products Inc.). The final assembly for heating was equivalent as to described above. Chips were heated to 750 °C ± 5 °C before being exposed to 100 sccm of CH_4 for 10 minutes to match the exposure times in full cell experiments. Clear evidence of carbon accumulation based on Raman spectra was apparent within ~3 minutes. Chips were then cooled under Ar with Raman spectra being acquired continuously to monitor compositional changes occurring under the inert atmosphere.

Results

Operando observations of differences in carbon tolerance

Coupling electrochemical methods with *operando* Raman spectroscopy has proven to be an effective method for measuring carbon tolerance,[53] as any accumulated carbon will give rise to a strong Raman vibrational feature at 1560 cm^{-1} as shown in Fig. 2. (The exact frequency of this band depends slightly on temperature.) This vibrational mode corresponds to highly ordered graphite on the cell surface and is often referred to as the "G-band". In addition to this feature, Raman vibrational modes at 1350 cm^{-1} and 2699 cm^{-1} assigned to disordered graphite ("D-band") and vibration-phonon coupling ("2-D band"), respectively, also appear in Fig. 2. (The lower frequency feature at ~600 cm^{-1} is due to the YSZ substrate.) Raman bands assignments and frequencies relevant to the present study are cited in Table 1. Correlating carbon accumulation

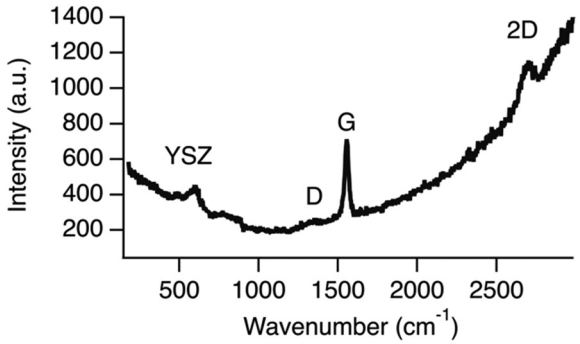

Fig. 2 Representative Raman spectrum of reduced Ni after exposure to CH_4. The G-band visible at 1560 cm^{-1} is used in this study to confirm carbon accumulation. This spectrum was acquired at 750° with an acquisition time of 30 s.

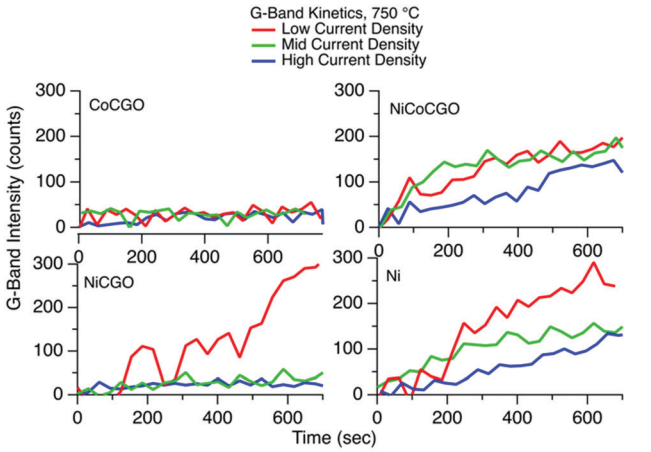

Fig. 3 Representative Raman kinetic traces of G-band appearance at 100% CH_4 conditions under all studied polarizations. CH_4 exposure started at time 0. While Co–CGO samples showed no sign of carbon accumulation under any conditions, carbon was continuously visible in Ni containing samples. Representative Raman spectra appear in ESI,† Fig. SI-1.

on anodes with changes in EIS and voltammetry data has provided insight into the effects of carbon on electrochemical oxidation, mass transport and material degradation.[16,32,48]

All experiments in this work were performed at 750 °C and carbon accumulation was monitored using mixtures of CO_2 and CH_4 at ratios of 30 : 70, 50 : 50, 75 : 25, and 0 : 100% CH_4. Every sample was exposed to the gas ratios at 85%, 40%, and 10% of each cell's maximum current (I_{max}) for 10 minutes each. These electrochemical conditions will be referred to as high, medium and low current conditions, respectively. In previous reports, a 10 minute exposure to CH_4 showed significant carbon accumulation on traditional Ni–YSZ cermet anodes.[6,7,54] Continuous Raman measurements were performed to track the growth of the G-band. Mixtures of CO_2 and CH_4 did not lead to any spectroscopically observable carbon on any of the cell surfaces; carbon was only observed with 100% CH_4 conditions. These results indicate that addition of CO_2 to the inlet fuel stream suppresses carbon accumulation and is consistent with several past studies showing that at temperatures above 700 °C, CO_2 in the incident fuel leads to dry reforming reactions that remove deposited carbon.[54–56] Dry reforming is thermodynamically favoured at temperatures above 730 °C assuming standard state partial pressures of reactants and products. As no carbon was observable even at the lowest CO_2 ratios (25%) in the current studies, our observations imply that CO_2 dry-reforming occurred faster than CH_4 decomposition and subsequent coking.

Fig. 3 shows Raman kinetic traces comparing carbon accumulation rates on all cells exposed to pure CH_4 at high, mid and low currents. The kinetic traces are a compilation of Raman scans collected every 30 seconds where the height of the G-band is measured individually from each spectrum. Changes in the kinetic data between cells having the same anode composition and tested at different current densities are the result of the different electrochemical polarization conditions driving more or fewer oxides to the anode. Comparing different samples operating with the same polarization conditions illustrate how effectively the infiltrated nanoparticles catalyze C–H bond activation.

Data in Fig. 3 show clearly that carbon accumulation occurred in all samples where Ni was present, even in combination with other infiltrates. This result emphasizes Ni's strong propensity towards C–H bond activation even when present only in small amounts. Several of the sharp features (or dips) in the Fig. 3 Raman data are a result of continuous re-focusing of the Raman microscope in order to maintain optimal signal intensity. While these features are more apparent in some samples than others, they do not change the general carbon accumulation trends. Samples infiltrated solely with Ni consistently showed the most carbon under all polarization conditions with counts exceeding 300 under low current conditions. (The "counts" label refers to the G-peak Raman intensity. Previous work from our lab has shown G-peak intensities correlate closely with the amount of electrochemically accessible accumulated carbon.[57]) Note that that the low nanoparticle loadings on the STN scaffolds did not provide sufficient percolation for the nanoparticles themselves to serve as a stand-alone SOFC anode.

Co-infiltrated Ni–CGO samples repeatedly showed little carbon formation at high and mid polarization, but increased carbon accumulation at low polarizations with counts just below 300. Comparing the Ni only and Ni–CGO samples illustrates that addition of CGO to the anode microstructure decreases the amount of deposited carbon This effect can be attributed both to CGO's relatively high ionic conductivity under reducing conditions, as well as its oxygen storage capacity (OSC). This effect was also observed for the bimetallic infiltrated sample, Ni–Co–CGO. While slight carbon accumulation was observed under each polarizing current, counts never exceeded 200 for these samples. With low current conditions Ni–Co–CGO anode showed even less carbon accumulation compared to Ni–CGO but carbon was nevertheless present. Co–CGO infiltrated anodes showed no signs of any observed carbon accumulation, even with 100% CH_4 conditions at low currents. While Co has been cited as a carbon tolerant electrocatalyst,[58,59] Co–CGO's poor electrochemical performance identified in these studies and illustrated in Fig. 4 implies that Co has very little catalytic activity towards C–H

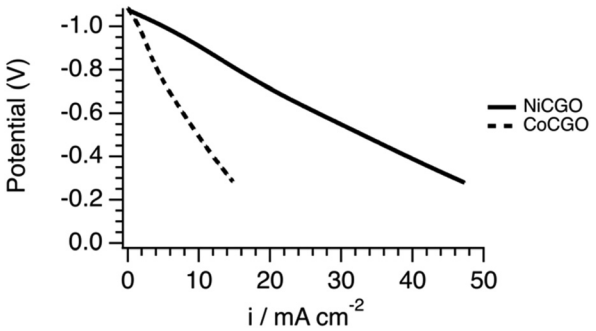

Fig. 4 Representative LSV traces of cell with Co–CGO anode compared to Ni–CGO anode measured in humidified H_2 at 750 °C.

bond activation. These findings caution against complete replacement of Ni with Co in the quest to develop high efficiency, carbon tolerant SOFC electrode materials.[37,60,61]

Infiltrated STN ceramic electrodes studied in this work were fabricated to decouple the electrocatalytic phase from the electronic conducting phase. This strategy has become popular in the quest to develop carbon tolerant MIEC materials for SOFC electrodes.[31,62,63] Infiltrates were added to the porous STN backbone in order to improve the materials' electrocatalytic capability. In order to compare carbon's tendency to accumulate on infiltrated STN electrodes relative to traditional Ni–YSZ cermet anodes comprised of μm sized Ni and YSZ particles,[64–67] equivalent experiments were performed using internally manufactured, electrolyte supported SOFCs having a Ni–YSZ cermet anode. Under pure methane conditions and low polarization, a standard Ni–YSZ anode showed more than double the counts of G-band intensity in the Raman spectra compared to the Ni based, nano-infiltrated anodes shown in Fig. 3. Traditional Ni–YSZ cermets also showed evidence of carbon deposition at low current conditions when exposed to a mixture of 75% CH_4 and 25% CO_2 (Fig. 5). While nano-infiltrated anodes do not show Raman signal above the noise limit (~20 counts) with this CH_4/CO_2 balance, an average of 60 counts and a clear G-peak was observed on the standard Ni–YSZ anode. Admittedly, the Ni–YSZ cermet anode had considerably higher Ni content than the Ni-infiltrated STN electrode, leading to greater susceptibility for carbon accumulation. Nevertheless, this comparison served its purpose in comparing carbon tolerances between the infiltrated ceramic electrodes designed to be carbon tolerant and a traditional SOFC anode. Furthermore, these studies show that even those electrodes having low Ni-content are susceptible to coking.

Carbon disappearance during cooling

Raman spatial sampling was used to examine the homogeneity of carbon deposition on the nano-infiltrated anodes with measurable G-band intensity. Fig. 6 shows a representative Raman spectrum collected at various locations across a Ni-CGO anode following final benchmark measurements at low current, 100% CH_4 conditions at 750 °C. The spectra show a homogenous distribution of carbon across the anode surface regardless of measurement location. While carbon is clearly present across the anodes at operating temperatures, no carbon signal was observed on these same samples after cool down under argon. Based on these findings, any analysis of the infiltrated STN electrodes used in this work based on *ex situ*, *post mortem* analyses would conclude that all electrodes other than the Ni-only infiltrated anode are carbon tolerant, despite the *operando* vibrational spectroscopy data that shows clear carbon accumulation on the Ni–CGO and Ni–Co–CGO during operation. Following disassembly and *post mortem* analysis, Raman signal from the STN-itself and anode infiltrates (CGO, primarily) were still visible, and *ex situ* SEM analysis showed no obvious changes in anode microstructure suggesting that carbon removal occurred without significant changes to other anode materials. In order to investigate this observation further, two Ni–CGO cells were independently heated up to 750 °C and exposed to CH_4 at low current conditions. Following carbon exposure and G-band appearance, fuel environments over both electrodes were switched to Ar in order to prevent carbon removal due to imperfect seals between the anode and cathode chambers and/or continued oxide diffusion through the electrolyte. Cells were cooled under these conditions and G-band intensities were monitored in order to identify any changes in accumulated carbon as the temperature returned to ambient conditions.

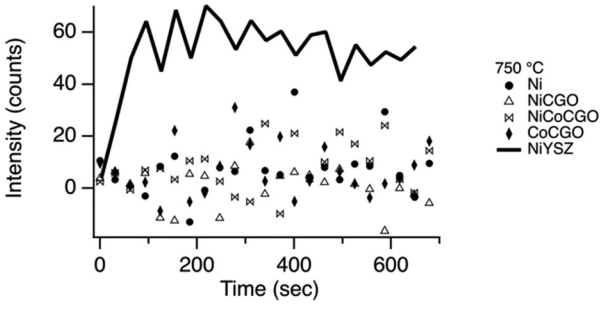

Fig. 5 Raman kinetics of G-band intensity upon exposure to a fuel mixture of 75% CH_4 and 25% CO_2. While nano-infiltrated catalysts do not show any sign of carbon deposition, a standard Ni–YSZ anode shows a stable G-band intensity of ~60 counts.

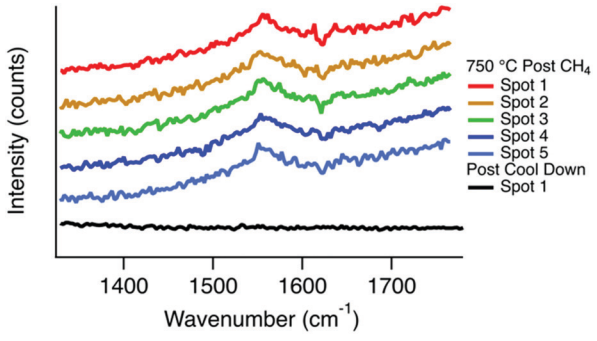

Fig. 6 Raman measurements with 30 s exposure time collected at various locations across Ni–CGO anode surface (average of 1 mm spacing) including close to fuel inlet, close to current collector, and anode edge and centre.

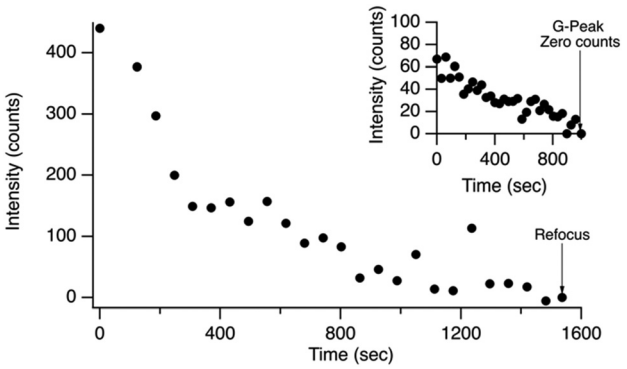

Fig. 7 Representative Raman kinetics of G-band intensity during cell cool down following Ni–CGO anode exposure to CH_4 at near OCV conditions. The inset shows kinetics following a Raman re-focus after the initial 1600 seconds.

Fig. 7 shows the changes in G-band intensity as a function of temperature as the Ni–CGO cells cooled. Cells were cooled at a rate of $\sim$2.5 °C min^{-1} and the total time in Fig. 7 (including top right inset) amounts to a ΔT of $\sim$−120 °C. After 25 minutes (1500 s) of cooling (anode temperature of $\sim$690 °C), very little intensity was observed in the G-band. A challenge when making these measurements was maintaining an optimal focus for the Raman excitation laser. As the temperature cooled, thermal expansion changed the sample height sufficiently to become a second source of signal loss. The microscope field of view was re-focused after 27 minutes to re-optimize G-band signal. While some signal was measurable ($\sim$80 counts) this number continued to decrease upon continued cooling (inset, Fig. 7). Because traditional Ni–YSZ and infiltrated Ni-only anodes both repeatedly show visible anode coking in *post mortem* analyses when cooled under equivalent conditions, carbon removal on the infiltrated samples must be explained by differences in material composition between the Ni-only, Ni–YSZ cermet anode and the nano-co-infiltrated STN. As STN is not catalytically active towards CH activation,[28] carbon related changes must be due to the infiltrates. In order to investigate whether carbon removal upon cool down was a result simply of Ni particle size, chip studies of nano-sized NiO were conducted. Co was not considered for these studies as Co–CGO infiltrated samples had proved carbon tolerant during operation. Fig. 8 shows Raman spectra of a NiO chip comprised of nano-sized particles. The peak at 500 cm^{-1}, a signature of nano-NiO,[49,68] confirms that the particles did not undergo significant coarsening during sintering. The difference in line width of the 500 cm^{-1} feature is attributed to thermal broadening. Fig. 8 shows clearly that carbon deposition occurs at 750 °C, and carbon remains during cool-down and during *post mortem* analysis. Therefore, carbon loss upon cool down cannot be attributed to differences in catalyst size.

Based on these observations, we attribute carbon disappearance from Ni–CGO and Ni–Co–CGO infiltrated anodes to the CGO itself. This material is the only apparent oxygen source in the infiltrated STN anodes as Ni and Co are both reduced to pure metal catalysts at the start of the study and then preserved

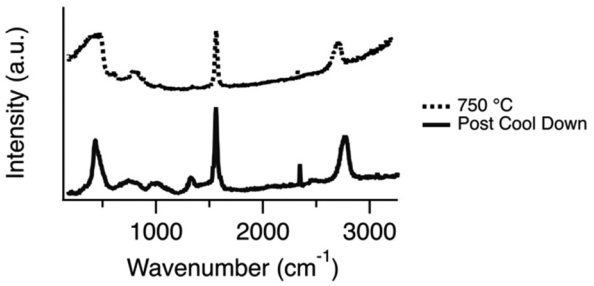

Fig. 8 Raman extended scans showing surface of nano-NiO chip after exposure to CH_4 at temperature and post cool down.

as zero-valent elemental materials during cool-down. CeO_2 based materials are widely used in a variety of catalyst applications because of their OSC. Ceria's well-known, labile Ce^{4+}/Ce^{3+} mixed valence at high temperatures and low P_{O_2} leads to MIEC capabilities.[69,70] Below 700 °C, CGO is nearly a pure ionic conductor[69,71,72] and these conditions, where little electronic conductivity is observed, could explain the observed Raman kinetics and the oxidation of carbon in the studied samples when temperatures approached 700 °C and below. Electronic conductivity would enable materials (such as elemental carbon) to remain reduced, while lack of electronic conductivity but continued ion conductivity could, conceivably provide a path leading to carbon oxidation. CGO's potential to oxidize carbon by active lattice oxygen species, even under low partial pressures of oxygen has been reported elsewhere.[73,74] Additionally, synergistic effects with Ni have been found to enhance the ability of ceria to oxidize carbon.[75]

To investigate CGO's role in C-removal, a sample consisting of nano-sized NiO (90%) and CGO (10%) was prepared and subjected to the same testing procedure as the nano-NiO chip described above. The results for the NiO–CGO chip show clearly that G-band intensity decreases dramatically between 700 °C and 675 °C, with no measurable G-band intensity at 650 °C (Fig. 9). Carbon disappearance coincides with a dramatic increase in the intensity of the CeO_2 F_{2g} Raman peak at 460 cm^{-1}. Fig. 10 shows measurements comparing the chip's surface composition prior to heat up (top trace) where NiO and CGO signals are prominent, after CH_4 exposure at 750 °C showing clear G-band intensity (middle trace), and after cool

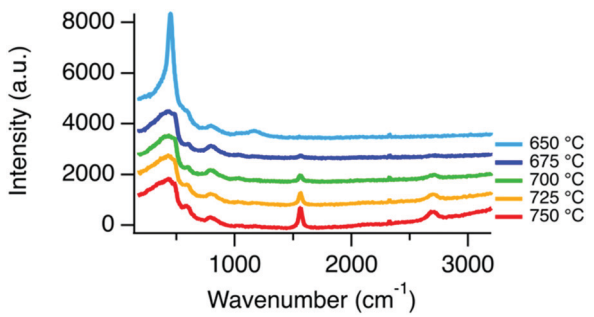

Fig. 9 Raman extended scans of nano NiO (90%) CGO (10%) chip taken during cool down to track changes in the G-band at $\sim$1560 cm^{-1}.

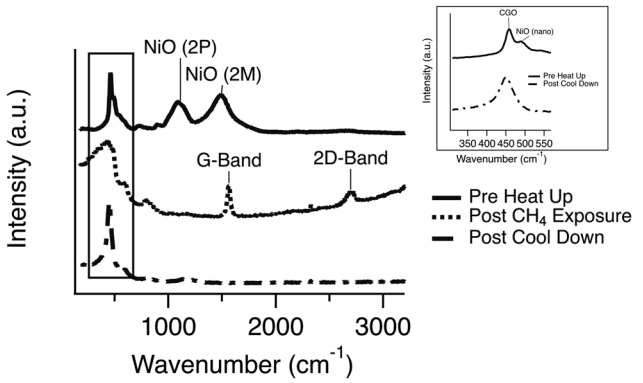

Fig. 10 Comparison of Raman extended scans of nano NiO (90%) and CGO (10%) chip prior to heat up, at 750 °C after CH_4 exposure and post cool down. Raman G-band present at temperature is not visible post cool down.

down (bottom trace). Curiously, the bottom trace of Fig. 10 shows no sign of Ni oxidation eliminating any suspicion of surface oxidation due to a leak or oxide flux through the sample. This result instead suggests a mechanism for carbon removal that utilizes labile oxygen in CGO, but these same species are not sufficiently labile to oxidize Ni, as evidenced by the absence of the NiO 2P peak in the spectrum post-cool down. Smaller CeO_2 nanoparticles support this theory as they exhibit even greater relative OSC given to their larger relative surface areas.[76] Comparing redox potentials of the $CO_2/C_{(s)}$ couple with that of NiO/Ni, thermodynamics predict that carbon would be preferentially oxidized when compared to Ni[77] as the equilibrium potential for the NiO/Ni couple is less favourable (−0.73 V) compared to that of the CO/CO_2 product couple (−0.99 V).[3,8] These predictions have been experimentally validated by several *in situ* studies.[20,53,78] We assume that had more carbon accumulated on the samples, such as the amounts seen on Ni–YSZ cermet-based cells, complete carbon oxidation might not have been possible, but a decrease in *post mortem* Raman signal compared to *operando* signals would still be expected. Studies claiming that CeO_2-based catalysts are carbon tolerant[37,38,40–43] should therefore consider carefully the chemistry that can occur during cool-down and how changes in catalyst reactivity might impact *post mortem* analyses relative to what is observed in direct, *operando* measurements.

Conclusions

Operando spectroscopic data presented above demonstrate that assumptions about SOFC electrode properties based on *ex situ* measurements may fail to capture relevant surface chemistry that occurs when carbon containing fuels are being electrochemically oxidized. Vibrational Raman data show the importance of acquiring real-time, materials-specific information about SOFC electrodes in order to determine anode carbon tolerance. In the present work a novel anode design based on infiltration of Ni, Co, and CGO into an STN backbone was investigated. All anodes tested in this study proved carbon tolerant when CO_2 was present in the fuel stream in combination with CH_4. Under pure CH_4 conditions all anodes except for ones infiltrated with Co–CGO showed that carbon accumulated at 750 °C. Carbon accumulation on the surface of these samples, however, was much less than that observed in Ni–YSZ cermet anodes. While the current study has proven that carbon will accumulate where Ni is present, quantifying the amount of carbon based on Ni particle size remains a challenge for future work. In addition to confirming carbon formation on the infiltrated STN anodes, results also demonstrated that CGO in the anode functioned as an oxygen reservoir upon cool down. This behaviour led to oxidation of the surface carbon present during cool down. While questions remain about how to improve the electrochemical performance of the studied cells to make them competitive with conventional SOFC materials, the increase in carbon tolerance can help drive future studies.

Conflicts of interest

There are no conflicts to declare.

Acknowledgements

RAW and MMW gratefully acknowledge support from the United States National Science Foundation (CHE-1710695). DBD, MLT, BRS and PH acknowledge colleagues at DTU Energy for technical assistance and fruitful discussions. Furthermore, the authors acknowledge financial support from the project ''BALANCE'' (European Union's Horizon 2020 Research and Innovation Program under grant agreement number 731224).

Notes and references

1 K. Kendall, *Int. Mater. Rev.*, 2005, **50**, 257–264.
2 C. Comminges, Q. X. Fu, M. Zahid, N. Y. Steiner and O. Bucheli, *Electrochim. Acta*, 2012, **59**, 367–375.
3 A. Faes, A. Hessler-Wyser, A. Zryd and J. Van Herle, *Membranes*, 2012, **2**, 585–664.
4 D. Sarantaridis and A. Atkinson, *Fuel Cells*, 2007, **7**(3), 246–258.
5 C. Song, *Catal. Today*, 2002, **77**, 17–49.
6 J. D. Kirtley, D. A. Steinhurst, J. C. Owrutsky, M. B. Pomfret and R. A. Walker, *Phys. Chem. Chem. Phys.*, 2014, **16**, 227–236.
7 M. D. McIntyre, J. D. Kirtley, D. M. Halat, K. W. Reeping and R. A. Walker, *ECS Trans.*, 2013, **57**, 1267–1275.
8 S. McIntosh and R. J. Gorte, *Chem. Rev.*, 2004, **104**, 4845–4866.
9 S. McIntosh, J. M. Vohs and R. J. Gorte, *J. Electrochem. Soc.*, 2003, **150**, A470.
10 M. Toebes, *Catal. Today*, 2002, **76**, 33–42.
11 M. Kogler, E.-M. Köck, M. Stöger-Pollach, S. Schwarz, T. Schachinger, B. Klötzer and S. Penner, *Mater. Chem. Phys.*, 2016, **173**, 508–515.
12 A. J. Jacobson, *Chem. Mater.*, 2010, **22**, 660–674.

13 J. Hanna, W. Y. Lee, Y. Shi and A. F. Ghoniem, *Prog. Energy Combust. Sci.*, 2014, **40**, 74–111.
14 N. M. Tikekar, T. J. Armstrong and A. V. Virkar, *J. Electrochem. Soc.*, 2006, **153**, A654.
15 K. Sasaki and Y. Teraoka, *J. Electrochem. Soc.*, 2003, **150**, A878.
16 G. J. Offer, J. Mermelstein, E. Brightman and N. P. Brandon, *J. Am. Ceram. Soc.*, 2009, **92**, 763–780.
17 H. He and J. M. Hill, *Appl. Catal., A*, 2007, **317**, 284–292.
18 W. Wang, H. Zhu, G. Yang, H. J. Park, D. W. Jung, C. Kwak and Z. Shao, *J. Power Sources*, 2014, **258**, 134–141.
19 X. Li, G. Shao, J. Luo, J. Lu, M. Xue, Y. Hou and L. Deng, *Mater. Res. Bull.*, 2014, **50**, 337–340.
20 M. D. McIntyre, J. D. Kirtley, A. Singh, S. Islam, J. M. Hill and R. A. Walker, *J. Phys. Chem. C*, 2015, **119**, 7637–7647.
21 S. Park, J. M. Vohs and R. J. Gorte, *Nature*, 2000, **404**, 265–267.
22 R. J. Gorte, S. Park, J. M. Vohs and C. Wang, *Adv. Mater.*, 2000, **12**, 1465–1469.
23 O. A. Marina, C. Bagger, S. Primdahl and M. Mogensen, *Solid State Ionics*, 1999, **123**, 199–208.
24 T. D. McColm and J. T. S. Irvine, *Ionics*, 2001, **7**, 116–121.
25 T. Ramos, C. Bernuy-Lopez, B. R. Sudireddy, J. J. Bentzen, W. Zhang, P. S. Jorgensen and L. T. Kuhn, *ECS Trans.*, 2012, **45**, 389–402.
26 T. Ramos, S. Veltzé, B. R. Sudireddy, P. S. Jørgensen, L. T. Kuhn and P. Holtappels, *Fuel Cells*, 2014, **14**, 1062–1065.
27 P. Blennow, K. K. Hansen, L. R. Wallenberg and M. Mogensen, *Solid State Ionics*, 2009, **180**, 63–70.
28 M. D. Gross, K. M. Carver, M. A. Deighan, A. Schenkel, B. M. Smith and A. Z. Yee, *J. Electrochem. Soc.*, 2009, **156**, B540–B545.
29 T. Ramos, S. Veltze, B. R. Sudireddy and P. Holtappels, *ECS Electrochem. Lett.*, 2013, **3**, F5–F6.
30 R. J. Gorte and J. M. Vohs, *Curr. Opin. Colloid Interface Sci.*, 2009, **14**, 236–244.
31 T. Z. Sholklapper, H. Kurokawa, C. P. Jacobson, S. J. Visco and L. C. De Jonghe, *Nano Lett.*, 2007, **7**, 2136–2141.
32 D. B. Drasbæk, M. L. Traulsen, R. A. Walker and P. Holtappels, *Fuel Cells*, 2019, **19**, 484–493.
33 B. C. H. Steele, P. H. Middleton and R. A. Rudkin, *Solid State Ionics*, 1990, **40–41**, 388–393.
34 R. J. Gorte and J. M. Vohs, *J. Catal.*, 2003, **216**, 477–486.
35 R. J. Gorte, *AIChE J.*, 2010, **56**, 1126–1135.
36 H. Zhong, H. Matsumoto and T. Ishihara, *Electrochemistry*, 2009, **77**, 155–157.
37 Y.-H. Huang, R. I. Dass, Z.-L. Xing and J. B. Goodenough, *Science*, 2006, **312**, 5.
38 A. Torabi and T. H. Etsell, *J. Electrochem. Soc.*, 2012, **159**, B714–B722.
39 H. Kan and H. Lee, *Catal. Commun.*, 2010, **12**, 36–39.
40 H. Kim, C. Lu, W. L. Worrell, J. M. Vohs and R. J. Gorte, *J. Electrochem. Soc.*, 2002, **149**, A247–A250.
41 B. Huang, X. Zhu, W. Hu, Y. Wang and Q. Yu, *J. Power Sources*, 2010, **195**, 3053–3059.
42 Z. Tao, G. Hou, N. Xu and Q. Zhang, *Int. J. Hydrogen Energy*, 2014, **39**, 5113–5120.
43 S.-I. Lee, K. Ahn, J. M. Vohs and R. J. Gorte, *Electrochem. Solid-State Lett.*, 2005, **8**, A48–A51.
44 P. Blennow, J. Hjelm, T. Klemensø, Å. H. Persson, S. Ramousse and M. Mogensen, *Fuel Cells*, 2011, **11**, 661–668.
45 M. B. Pomfret, C. Stoltz, B. Varughese and R. A. Walker, *Anal. Chem.*, 2005, **77**, 1791–1795.
46 M. B. Pomfret, J. C. Owrutsky and R. A. Walker, *Annu. Rev. Anal. Chem.*, 2010, **3**, 151–174.
47 D. A. Agarkov, I. N. Burmistrov, F. M. Tsybrov, I. I. Tartakovskii, V. V. Kharton and S. I. Bredikhin, *Solid State Ionics*, 2017, **302**(Suppl. C), 133–137.
48 R. C. Maher, L. F. Cohen, P. Lohsoontorn, D. J. L. Brett and N. P. Brandon, *J. Phys. Chem. A*, 2008, **112**, 1497–1501.
49 N. Mironova-Ulmane, A. Kuzmin, I. Sildos, L. Puust and J. Grabis, *Latv. J. Phys. Tech. Sci.*, 2019, **56**, 61–72.
50 P. Klar, E. Lidorikis, A. Eckmann, I. A. Verzhbitskiy, A. C. Ferrari and C. Casiraghi, *Phys. Rev. B: Condens. Matter Mater. Phys.*, 2013, **87**, 205435.
51 V. Alzate-Restrepo and J. M. Hill, *Appl. Catal., A*, 2008, **342**, 49–55.
52 B. C. Eigenbrodt, M. B. Pomfret, D. A. Steinhurst, J. C. Owrutsky and R. A. Walker, *J. Phys. Chem. C*, 2011, **115**, 2895–2903.
53 J. D. Kirtley, D. M. Halat, M. D. McIntyre, B. C. Eigenbrodt and R. A. Walker, *Anal. Chem.*, 2012, **84**, 9745–9753.
54 J. D. Kirtley, M. B. Pomfret, D. A. Steinhurst, J. C. Owrutsky and R. A. Walker, *J. Phys. Chem. C*, 2015, **119**, 12781–12791.
55 A. Lanzini, P. Leone, C. Guerra, F. Smeacetto, N. P. Brandon and M. Santarelli, *Chem. Eng. J.*, 2013, **220**, 254–263.
56 J. Staniforth and R. M. Ormerod, *Ionics*, 2003, **9**, 336–341.
57 J. D. Kirtley, M. D. McIntyre, D. M. Halat and R. A. Walker, *ECS Trans.*, 2013, **50**, 3–15.
58 O. Costa-Nunes, R. J. Gorte and J. M. Vohs, *J. Power Sources*, 2005, **141**, 241–249.
59 P. Boldrin, E. Ruiz-Trejo, J. Mermelstein, J. M. Bermúdez Menéndez, T. Ramírez Reina and N. P. Brandon, *Chem. Rev.*, 2016, **116**, 13633–13684.
60 Y. Lin, Z. Zhan and S. A. Barnett, *J. Power Sources*, 2006, **158**, 1313–1316.
61 H. Li, Y. Tian, Z. Wang, F. Qie and Y. Li, *RSC Adv.*, 2012, **2**, 3857.
62 A. Tschöpe, E. Sommer and R. Birringer, *Solid State Ionics*, 2001, **139**, 255–265.
63 N. Laosiripojana and S. Assabumrungrat, *Chem. Eng. Sci.*, 2006, **61**, 2540–2549.
64 S. P. Jiang, *Int. J. Hydrogen Energy*, 2012, **37**, 449–470.
65 S. P. Jiang, S. Zhang, Y. D. Zhen and W. Wang, *J. Am. Ceram. Soc.*, 2005, **88**, 1779–1785.
66 S. P. Jiang, X. J. Chen, S. H. Chan and J. T. Kwok, *J. Electrochem. Soc.*, 2006, **153**, A850–A856.
67 W. Wang, S. P. Jiang, A. I. Y. Tok and L. Luo, *J. Power Sources*, 2006, **159**, 68–72.
68 N. Mironova-Ulmane, A. Kuzmin, I. Steins, J. Grabis, I. Sildos and M. Pärs, *J. Phys.: Conf. Ser.*, 2007, **93**, 012039.

69 S. P. S. Badwal, D. Fini, F. T. Ciacchi, C. Munnings, J. A. Kimpton and J. Drennan, *J. Mater. Chem. A*, 2013, **1**, 10768–10782.
70 B. C. H. Steele, *Solid State Ionics*, 2000, **129**, 95–110.
71 R. M. Batista, A. M. D. C. Ferreira and E. N. S. Muccillo, *Ionics*, 2016, **22**, 1159–1166.
72 D. Kashyap, P. K. Patro, R. K. Lenka, T. Mahata and P. K. Sinha, *Ceram. Int.*, 2014, **40**, 11869–11875.
73 M. Mogensen and K. Kammer, *Annu. Rev. Mater. Res.*, 2003, **33**, 321–331.
74 A. Trovarelli, *Catal. Rev.*, 1996, **38**, 439–520.
75 Q. Zhuang, Y. Qin and L. Chang, Promoting Effect of Cerium Oxide in Supported Nickel Catalyst for Hydrocarbon Steam-Reforming, *Appl. Catal.*, 1991, **70**, 1–8.
76 H. Imagawa, A. Suda, K. Yamamura and S. Sun, *J. Phys. Chem. C*, 2011, **115**, 1740–1745.
77 P. Atkins, T. Overton, J. Rourke, M. Weller, F. Armstrong and M. Hagerman, *Shriver & Atkins' Inorganic Chemistry*, W. H. Freeman and Company, New York, 5th edn, 2010.
78 J. Kirtley, A. Singh, D. Halat, T. Oswell, J. M. Hill and R. A. Walker, *J. Phys. Chem. C*, 2013, **117**, 25908–25916.